

Silicon spreading in δ -doped GaAs(100): A high-resolution electron-energy-loss-spectroscopy study

V. M. Polyakov and A. Elbe

Fachbereich Physik, Universität Kassel, D-34132 Kassel, Germany

J. Wu and G. J. Lapeyre

Department of Physics, Montana State University, Bozeman, Montana 59717

J. A. Schaefer

Institut für Physik, Technische Universität Ilmenau, D-98684 Ilmenau, Germany

(Received 7 June 1995)

High-resolution electron-energy-loss spectroscopy was applied to analyze in detail the spatial distribution of dopants in δ -doped (Si) GaAs(100) samples, molecular-beam epitaxially grown at 550 °C with different doping levels and depths. The fitting of the measured energy-loss spectra, based on a smooth self-consistent electron-density profile, reveals that at this growth temperature the silicon atoms are spread symmetrically around the initial doping plane for the doping level of $N_{\text{Si}}=1.3\times 10^{13}\text{ cm}^{-2}$. However, the asymmetry in the dopant spreading becomes appreciable for the higher doped sample with $N_{\text{Si}}=6\times 10^{13}\text{ cm}^{-2}$. In this case different diffusion coefficients of the dopant atoms were assumed in the growth direction and backward from the initial doping plane in order to obtain better fits to the measured energy-loss spectra. It was found that the damping of the plasmon excitations Γ changes versus a variation of the primary electron-beam energy E_0 with a significant decrease for the lowest primary energy applied. The observed dependence of Γ on E_0 is connected with the dominant optical phonon scattering, mostly contributing to the plasmon damping at room temperature. [S0163-1829(96)00427-4]

I. INTRODUCTION

Using epitaxial deposition methods it is now possible to follow the trend towards increasing miniaturization of devices. As there are ever greater demands on the control of materials preparation on length scales where quantum mechanical effects become relevant, preparation techniques on an atomic scale need to be developed. One important requirement is the ability to control the distribution of dopant atoms in the grown structures.

In this paper we study the dopant incorporation behavior of Si into GaAs(100) samples grown by molecular-beam epitaxy (MBE) with *in situ* high-resolution electron-energy-loss spectroscopy (HREELS). This study has been motivated by investigations of δ -doped semiconductors by virtue of different techniques as secondary-ion mass spectrometry (SIMS),¹⁻⁷ magnetotransport measurements,⁸ capacitance-voltage (*C-V*) profiling,⁹⁻¹¹ and Raman spectroscopy.¹² Investigations by HREELS (Refs. 13 and 14) demonstrated that this very surface-sensitive technique may provide information on spatial donor spreading and free-carrier density profiles of δ -doped layers in the vicinity of the surface, whereas other techniques mentioned above are limited when applying to the near-surface region.

In the present work we investigated δ -doped (Si) GaAs(100) samples at different doping levels and doping depths by virtue of the surface collective excitations (optical phonons and plasmons), observed in HREELS measurements. The measured energy-loss spectra are fitted with theoretical spectra. We used the symmetric rectangular-shaped dopant profile for the low-doped samples in order to calcu-

late self-consistent electron-density profiles, whereas for the high-doped structure the asymmetric Gaussian-shaped dopant distribution was applied. To take into account the dispersion of the quasi-two-dimensional plasmon excitations the long-wavelength approach of the Lindhard dielectric response function was exploited.

Further, we discuss the significant change of the plasmon damping versus the primary electron-beam energy with emphasis on the optical-phonon scattering mechanism of free electrons.

The remainder of our paper is outlined as follows. First, we describe in Sec. II the details of the experimental procedures in our HREELS measurements. The effective-mass approximation that we adopted for a calculation of the self-consistent electron-density profile along with the dipole scattering approach to compute the energy-loss spectra is summarized in Sec. III. The simplified three-layer model of the polar semiconductor, including the lattice vibrations, is considered in Sec. IV A to emphasize the main parameters of δ -doped structures, which influence the HREELS spectra. Section IV B contains the fitting results of HREELS spectra for low- and high-doped samples, based on the symmetric rectangular-shaped and asymmetric Gaussian-shaped distribution of dopants with the inclusion of the spatial dispersion of the plasmon mode. We discuss qualitatively the competition of different scattering mechanisms of the plasmon excitations. Finally, Sec. V briefly summarizes the present study.

II. EXPERIMENTAL PROCEDURE

All measurements have been carried out at the Center for Research in Surface Science and Submicron Analysis

(CRISS), Department of Physics, Montana State University, δ -doped (Si) samples of GaAs were grown in a Perkin-Elmer MBE system. Semi-insulating GaAs(100) wafer pieces with a size approximately 1 cm \times 1 cm were used as a substrate, which was stucked with indium on a (molybdenum) sample holder. Each sample contains a MBE-grown undoped GaAs buffer layer of 0.4- μ m thickness and a single δ layer at different depths beneath the surface.

During deposition of the Si atoms, GaAs growth was interrupted, but the As shutter kept open. The growth rate for GaAs was 0.27 μ m/h for the low-doped samples 10 and 11 and 0.43 μ m/h for the high-doped sample 17, obtained from RHEED (reflection high-electron energy diffraction) oscillation curves. The substrate temperature was 550 $^{\circ}$ C, the As/Ga ratio of 8 was determined with a Quadrupole Mass Spectrometer. The temperature of the Si effusion cell was 1165 $^{\circ}$ C, which corresponds to a Si flux of 1×10^{11} cm $^{-2}$ s $^{-1}$ known from the free-carrier concentration obtained (with this Si temperature and 0.43 μ m/h growth rate) for homogeneously doped GaAs samples from HREELS spectra. The δ -doped samples have a Si-sheet-doping concentration N_{Si} of 1.3×10^{13} and 6×10^{13} cm $^{-2}$ for low and high doping, respectively.

Our MBE growth chamber is connected with the analyzer via an UHV transfer system. That is of a great advantage to avoid heating δ -doped samples to 350–400 $^{\circ}$ C to decap an As-passivation overlayer, which certainly affects the initial Si-dopant profile. Our HREELS spectra as measured *in situ* show the original state of the δ -doped samples just after the MBE growth.

The analysis chamber is equipped with a HREELS spectrometer (Leybold-ELS-22 type), low-energy electron diffraction (LEED), Auger electron spectroscopy (AES), and x-ray and ultraviolet photoelectron spectroscopy (XPS, UPS). The analysis chamber is pumped by an ion pump and a turbo-molecular pump and had a base pressure of 1×10^{-10} mbar. All samples showed a (2 \times 4) RHEED pattern during the growth and a very clear $c(4 \times 4)$ LEED pattern (due to the excess of As in the growth chamber) after the growth.

HREELS spectra were measured in specular geometry with primary electron-beam energies ranging from 0.5 to 20 eV at an incidence angle of 45 $^{\circ}$. The energy resolution was chosen to be 8 meV, obtained from the full width at half maximum (FWHM) of the quasielastic peak of the undoped and homogeneously high-doped (Si) GaAs(100) samples.

III. MODEL DESCRIPTION

To calculate theoretically HREELS spectra for the δ -doped structures a knowledge of the electron-density profile is needed. In δ -doped n -type GaAs the silicon atoms are spread within the region from several tens to a few hundred Å centered in the vicinity of the intended ideal doping plane. The electrons, released from silicon atoms, experience the Coulomb interaction with their parent ionized donors, which leads to a confinement of electrons in the potential well, formed by dopants. If the confining potential appears to be strong enough, the electron de Broglie wavelength is comparable to the width of the potential well. As a result, the electron motion in a direction perpendicular to the surface is quantized and the energy subband structure is formed.

In order to obtain the electron-density profile we adopt the effective-mass approximation in the slab geometry.¹⁵ We consider a slab of GaAs with a thickness L large enough to mimic a semi-infinite geometry of the sample. Then, the electrons in the conduction band are treated as a free-electron gas with effective mass m^* , and the positive background of ionized dopants is presented by two Gaussians or rectangles, placed at equal depths beneath both sides of the slab. These symmetric conditions greatly reduce the diagonalization time of the matrix of the Schrödinger equation and do not influence the final results, since we need only the electron-density profile on the left side of the slab. The band bending is taken into account by placing two thin sheets of charge with areal charge densities $N_S^{(R)}$ and $N_S^{(L)}$ on the right and the left slab surfaces, taken equal for the same reason mentioned above. Additionally, we impose the infinite barrier heights at both slab surfaces to enforce the wave function of electrons to vanish just outside the slab. The latter boundary conditions are appropriate because the characteristic length scale of, at least, a few tens of Å is larger than the penetration depth of the electron wave function outside the surface.¹⁵

We consider overall electrical neutrality of the sample. Thus, if $n(z)$ is the volume electron density at a depth z we have

$$n_{\text{tot}} = \int_b^L n_D(z) dz + 2N_S,$$

where $N_{\text{tot}} = \int_0^L n(z) dz$ is the overall electron density inside the slab, $n_D(z)$ is the z -dependent ionized donor density, and $N_S = N_S^{(L)} = N_S^{(R)}$.

In that case the wave function of an electron in the conduction band is given by

$$\Psi_{\mathbf{q}_{\parallel}, i}(\mathbf{x}_{\parallel}, z) = \frac{1}{\sqrt{A}} \exp(i\mathbf{q}_{\parallel}\mathbf{x}_{\parallel}) \Phi_i(z),$$

where \mathbf{x}_{\parallel} and \mathbf{q}_{\parallel} are position and wave vectors in the plane parallel to the surface. Then, the energy eigenvalues are expressed as

$$E_i(\mathbf{q}_{\parallel}) = \frac{\hbar^2 q_{\parallel}^2}{2m^*} + \varepsilon_i.$$

The envelope wave functions $\Phi_i(z)$ and the energy eigenvalues ε_i are found from the one-dimensional Schrödinger equation

$$\left[-\frac{\hbar^2}{2m^*} \frac{d^2}{dz^2} + V_{\text{eff}}(z) \right] \Phi_i(z) = \varepsilon_i \Phi_i(z), \quad (1)$$

where the effective potential $V_{\text{eff}}(z)$ is given by

$$V_{\text{eff}}(z) = V_H(z) + V_{\text{xc}}(z).$$

The Hartree potential $V_H(z)$ is a self-consistent potential, which is found from the Poisson equation

$$\frac{d^2 V_H(z)}{dz^2} = -\frac{4\pi e^2}{\varepsilon_{\infty}} [n_D(z) - n(z)]. \quad (2)$$

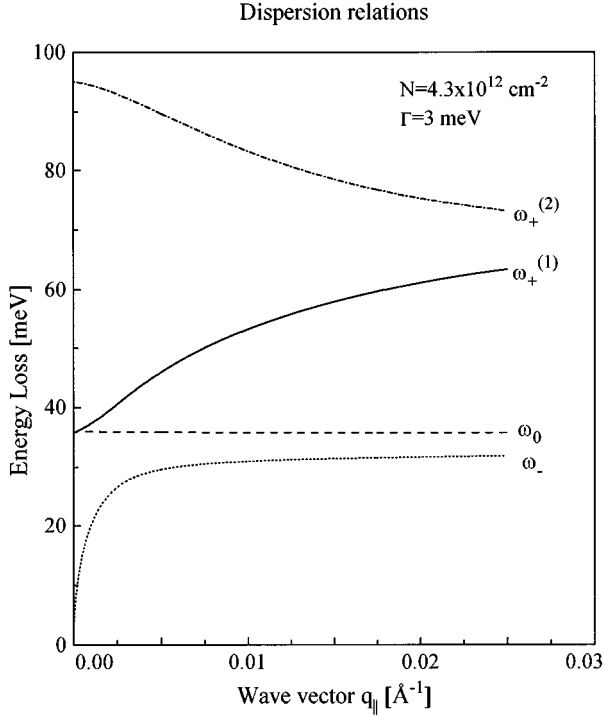


FIG. 1. Calculated dispersion relations of the main four plasmons ω_- , ω_0 , $\omega_+^{(1)}$, and $\omega_+^{(2)}$. A three-layer model of a polar semiconductor is composed of the depletion overlayer with 100-Å thickness, followed by uniformly n -doped interlayer with 75-Å thickness and a semi-infinite undoped substrate. The areal electron density of the interlayer $N=4.3 \times 10^{12} \text{ cm}^{-2}$ and the Drude dielectric function of the free-electron gas with the plasmon damping $\Gamma=3 \text{ meV}$ were chosen in the calculations.

We adopt the exchange-correlation potential $V_{xc}(z)$, expressed in a simple analytical form by Hedin and Lundqvist¹⁶

$$V_{xc}(z) = -\frac{2}{\pi \alpha r_s} \text{Ry}^* \left[1 + 0.7734 \ln \left(1 + \frac{1}{x} \right) \right],$$

with

$$\alpha = \left(\frac{4}{9\pi} \right)^{1/3}, \quad x(z) = \frac{r_s(z)}{21}, \quad r_s(z) = \left[\frac{4}{3} \pi (a^*)^3 n(z) \right]^{-1/3},$$

$$a^* = \frac{\varepsilon_\infty \hbar^2}{m^* e^2}, \quad \text{Ry}^* = \frac{e^2}{2\varepsilon_\infty a^*}.$$

Given the energy eigenvalues and corresponding envelope wave functions the electron density at a depth z is expressed by

$$n(z) = \frac{m^*}{\pi \hbar^2 \beta} \sum_i \ln[1 + e^{-\beta(\varepsilon_i - \mu)}] |\Phi_i(z)|^2,$$

with $\beta=1/k_B T$ and μ the chemical potential. The chemical potential is found from the criterion of the overall neutrality of the slab

$$N_{\text{tot}} = \int_0^L n(z) dz = \int_0^L n_D(z) dz + 2N_S.$$

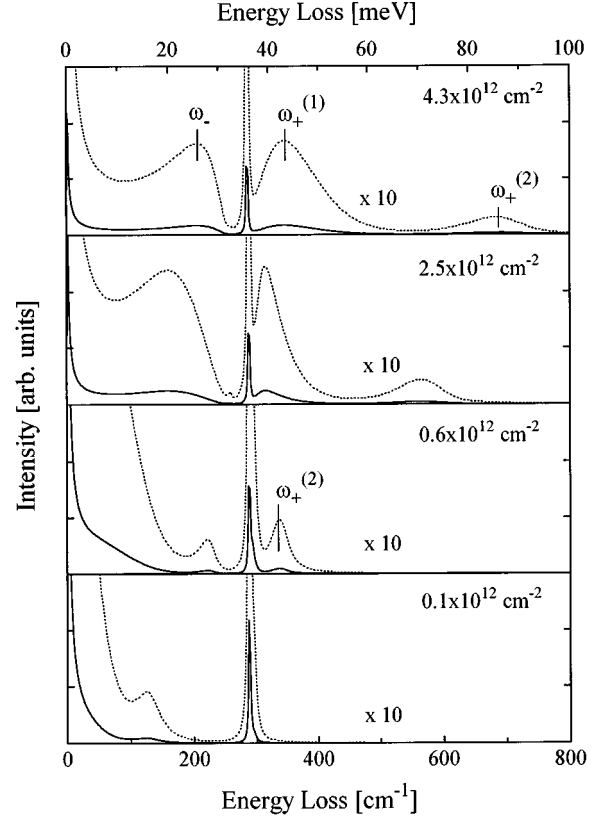


FIG. 2. Energy-loss probabilities $P_{el}(\omega)$ [Eq. (5)] for the three-layer model for different doping levels. The calculations were performed for a primary electron-beam energy $E_0=9 \text{ eV}$ and a plasmon damping $\Gamma=6 \text{ meV}$. Note the same vertical scale in all panels.

We solve self-consistently the Schrödinger and Poisson equations by virtue of real-space method, where the Eqs. (1) and (2) are approximated by finite-difference expressions, obtained on the discrete mesh of points within the interval $(0, L)$.

Calculated in this manner the electron-density profile is then discretized into a histogram of a finite number of sublayers in order to derive the effective dielectric function by virtue of a continued-fraction expansion^{17,18}

$$\varepsilon_{\text{eff}}(q_{\parallel}, \omega) = a_1 - \frac{b_1^2}{a_1 + a_2 - \frac{b_2^2}{a_2 + a_3 - \dots}}, \quad (3)$$

with $a_i = \varepsilon_i(q_{\parallel}, \omega, z) \coth(q_{\parallel} d_i)$ and $b_i = \varepsilon_i(q_{\parallel}, \omega, z) \sinh(q_{\parallel} d_i)$, where ε_i and d_i are the dielectric function and the thickness of the i th layer, respectively.

For our purpose we choose the long-wavelength limit¹⁹ of the Lindhard dielectric function²⁰ of the electron gas in order to take into account the dispersion of the plasmon excitations. Finally, the dielectric function of every sublayer in Eq. (3) takes the form

$$\varepsilon_i(q_{\parallel}, \omega, z) = \varepsilon_\infty + \frac{(\varepsilon_0 - \varepsilon_\infty) \omega_{\text{TO}}^2}{\omega_{\text{TO}}^2 - \omega^2 - i\gamma\omega} - \frac{\omega_p^2}{\omega^2 - D(q_{\parallel}) + i\Gamma\omega} \quad (4)$$

with $D(q_{\parallel}) = \frac{3}{5} v_F^2 q_{\parallel}^2$ and $\omega_p^2 = 4\pi e^2 n(z)/m^*$, where γ and Γ are the phonon and plasmon damping factors, respectively,

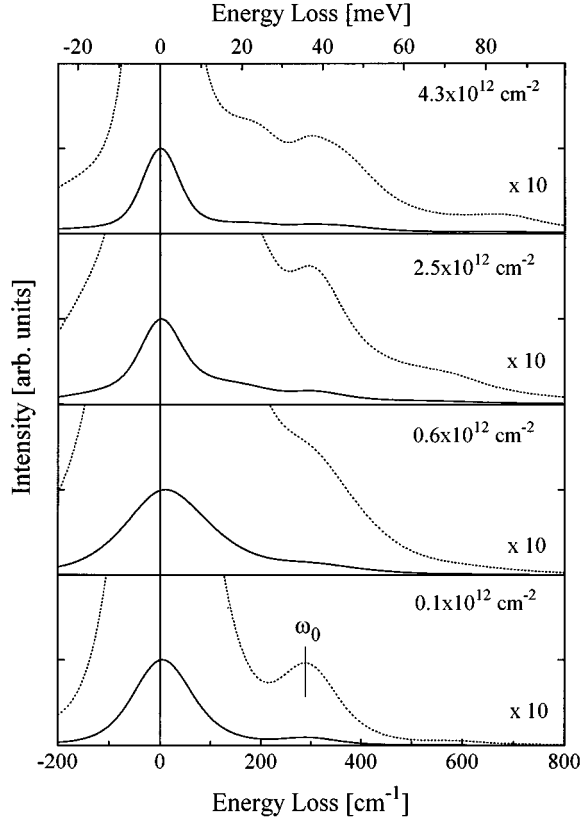


FIG. 3. The full energy-loss spectra, calculated for the same parameters as in Fig. 2. For the lowest doping level $N=0.1 \times 10^{12} \text{ cm}^{-2}$ the phonon peak at ω_0 energy is well resolved.

$\omega_{\Gamma 0}$ is the transverse optical phonon frequency. The contribution from the lattice vibrations is presented in Eq. (4) by the second term, and the first one, ϵ_∞ , has its origin from the polarization of the bound electrons.

Given the effective dielectric function the energy-loss probability $P_{\text{el}}(\omega)$ in the dipole scattering theory is calculated as¹⁷

$$P_{\text{el}}(\omega) = \frac{4e^2 \nu_\perp^2 k_S}{\pi^2 \hbar^2 k_I} \int_{|\mathbf{q}_\parallel| < q_\parallel^c} \frac{|\mathbf{q}_\parallel| d^2 \mathbf{q}_\parallel}{[\nu_\perp^2 q_\parallel^2 + (\omega - \nu_\parallel \mathbf{q}_\parallel)^2]} \times \text{Im} \left[\frac{-1}{\epsilon_{\text{eff}}(\mathbf{q}_\parallel, \omega) + 1} \right]. \quad (5)$$

Convolved with an appropriate instrumental function with the inclusion of the multiple energy losses and temperature dependence of the scattering target this value is compared with measured HREELS spectra.

IV. RESULTS AND DISCUSSION

A. Three-layer model for a polar semiconductor

For a better understanding of the main features of δ -doped structures we first consider the simplified model for a polar semiconductor. This model is assumed to be composed of the undoped overlayer with a thickness of 100 Å followed by a homogeneously doped slab with a thickness of 75 Å and a semi-infinite substrate. The embedded doped slab mimics a δ layer of finite width with a confined free-electron gas. Thus,

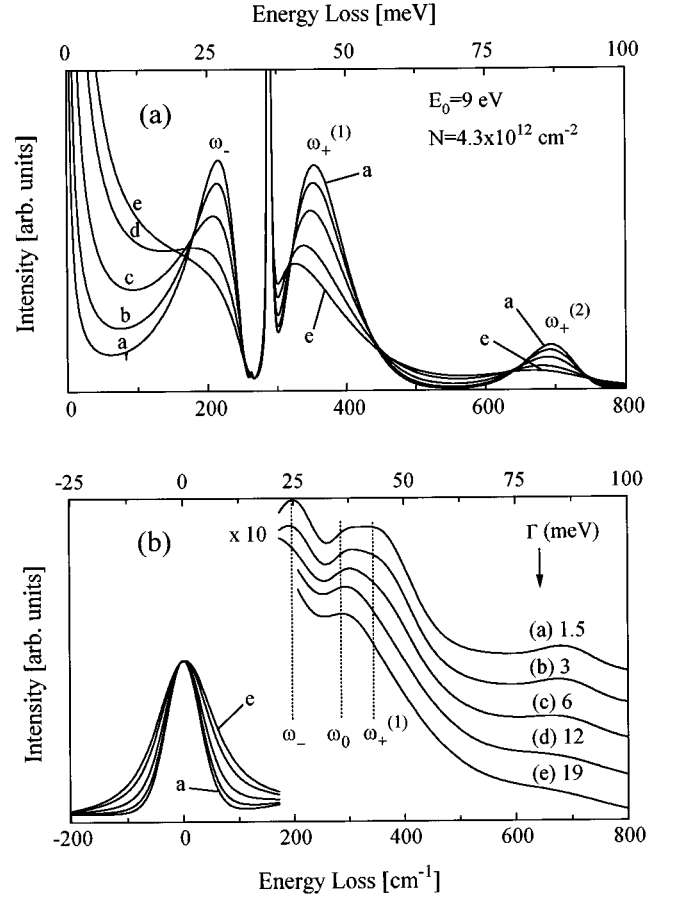


FIG. 4. Energy-loss probabilities $P_{\text{el}}(\omega)$ [panel (a)] and the full energy-loss spectra [panel (b)], calculated for different values of plasmon damping Γ , ranging from 1.5 to 19 meV. The curves in panel (a) are displayed from top to bottom for increasing plasmon damping as labeled in panel (b).

the overlayer and the semi-infinite substrate contribute to the energy-loss function only by virtue of phonon excitations, whereas in the doped slab a plasmon mode can be excited as well. The Drude model for the dielectric response function of the electron gas in the slab is assumed.

The poles of the surface loss function $\text{Im}\{-1/[\epsilon_{\text{eff}}(\mathbf{q}_\parallel, \omega) + 1]\}$ in Eq. (5) gives four main loss features, labeled as ω_- , ω_0 , $\omega_+^{(1)}$, and $\omega_+^{(2)}$ in Fig. 1, where the dispersion relations are shown. The appearance of two additional branches, if compared to the case of the neglect of the lattice vibrations,¹³ has the origin from the coupling between the phonon and plasmon excitations, which forms the intermixed modes or plasmarens.^{21–23} As q_\parallel increases, the branches $\omega_+^{(1)}$ and $\omega_+^{(2)}$ approach the value $\omega_p / (2\epsilon_\infty)^{1/2}$, appropriate to an energy of the “interface” plasmon. In the long-wavelength limit $q_\parallel \rightarrow 0$ the energy of the mode $\omega_+^{(2)}$ should be approximately $\omega_p / (\epsilon_\infty + 1)^{1/2}$, the surface plasmon energy with no depletion layer. The energy of the mode $\omega_+^{(1)}$, when $q_\parallel \rightarrow 0$, approaches the value ω_{LO} , the energy of the longitudinal optical phonon. It should be noted that the Drude dielectric function for the embedded electron gas predicts downward dispersion of the loss feature $\omega_+^{(2)}$, whereas the inclusion of the spatial dispersion results in upward curvature of both dispersion curves for $\omega_+^{(1)}$ and $\omega_+^{(2)}$ modes, re-

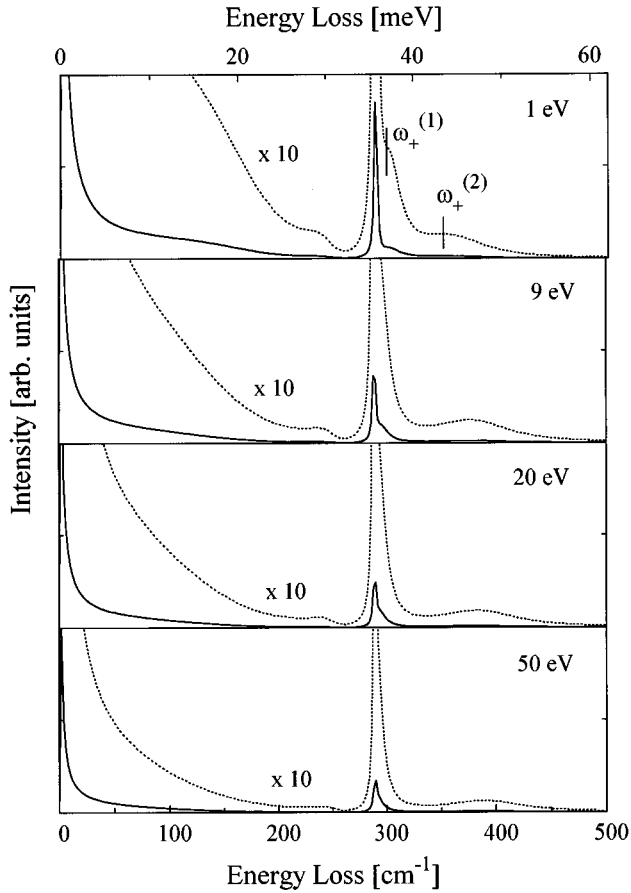


FIG. 5. The dependence of the energy-loss probability $P_{el}(\omega)$ on the primary electron-beam energy E_0 . The doping level $N=0.9 \times 10^{12} \text{ cm}^{-2}$ and the plasmon damping $\Gamma=12 \text{ meV}$ were used in the calculations. The vertical scale is the same for all panels.

spectively, which approach each other asymptotically with the increase of q_{\parallel} (not shown here).

We calculated the energy-loss spectra for this structure for different doping levels N and primary beam energies. The calculated energy-loss probabilities $P_{el}(\omega)$ for the set of doping levels ranging from 0.1×10^{12} to $4.3 \times 10^{12} \text{ cm}^{-2}$ (for the same primary beam energy $E_0=9 \text{ eV}$ and the plasmon damping $\Gamma=6 \text{ meV}$) are presented in Fig. 2. As one can see the energy of the acousticlike plasmon mode ω_- shifts downward with a decrease of the doping level. At high doping levels this peak is well resolved (Fig. 2, $N=4.3 \times 10^{12} \text{ cm}^{-2}$), but for further lowering of the doping level the plasmon mode ω_- no longer manifests itself as a single peak, but merges with a broad structureless feature in the vicinity of zero-energy losses, drastically broadening the elastic peak (Fig. 3, $N=0.6 \times 10^{12} \text{ cm}^{-2}$). The bare phonon ω_0 in this case is visible only as a weak shoulder of the elastic peak. Further decrease of the doping level to $0.1 \times 10^{12} \text{ cm}^{-2}$ leads to the narrowing of the elastic peak and accordingly to the sharpening of the phonon peak (bottom panel in Fig. 3). In the limit of a negligible doping one simply obtains the undoped structure with a narrow elastic peak and a well-resolved optical phonon ω_0 . It is worth mentioning that for the broadest elastic peak (doping level $N=0.6 \times 10^{12} \text{ cm}^{-2}$ in Fig. 3) its maximum is shifted appreciably from zero energy due to the large contribution from the structureless loss feature ω_- in this doping regime.

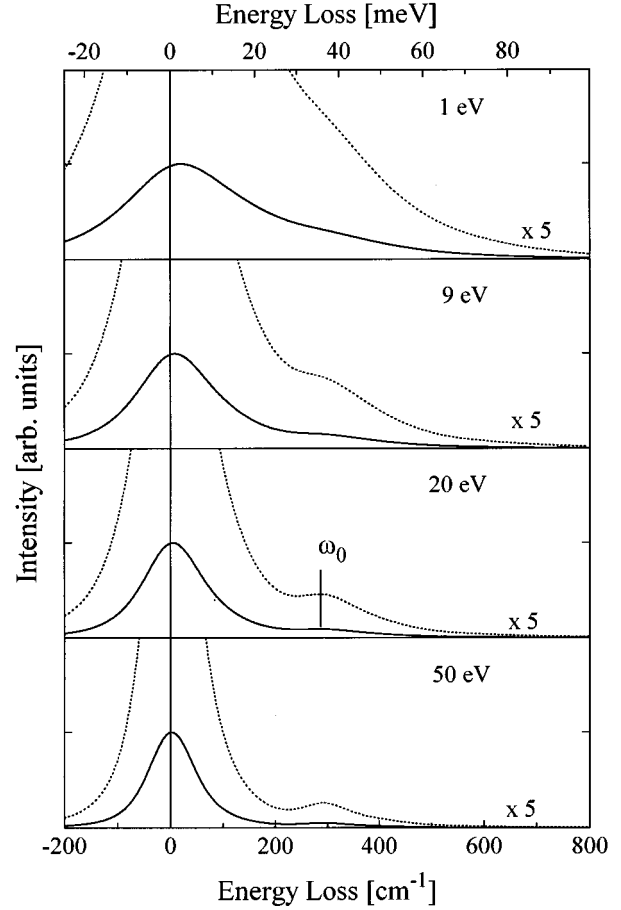


FIG. 6. The line-shape change of the full energy-loss spectrum with a variation of primary beam energy E_0 . The parameters used in the calculations are the same as in Fig. 5.

To elucidate the role of plasmon damping we calculated energy-loss spectra for the same model, varying a plasmon damping factor in the range from 3 to 19 meV (Fig. 4). The doping level was $4.3 \times 10^{12} \text{ cm}^{-2}$ and the primary beam energy was 9 eV, they were the same for all spectra. The increase of the plasmon damping causes the downward shift of the plasmon peak $\omega_+^{(1)}$ towards the phonon ω_0 [Fig. 4(a)] whereas the plasmon at ω_- gradually flattens and is almost buried in the elastic peak, increasing slightly its FWHM [Fig. 4(b)]. As a result of such behavior of the plasmon modes (instead of a good resolution of the plasmon ω_- and the phonon ω_0 for low damping), we obtain the single superimposed loss feature positioned at the energy of the bare phonon ω_0 with a large background, originating from the plasmons ω_- and $\omega_+^{(1)}$ [Fig. 4(b)]. This perturbed phonon we observed in all our measured energy-loss spectra.

The line-shape change of the calculated energy-loss spectra versus the primary energy for the doping level of $0.9 \times 10^{12} \text{ cm}^{-2}$ and the plasmon damping of 12 meV is shown in Fig. 6. For the lowest primary beam energy of 1 eV the elastic peak is strongly broadened due to the contribution from the low-energy structureless feature (Fig. 5). With the increase of the primary beam energy this contribution gradually decreases and the phonon peak evolves from the weak shoulder for $E_0=1 \text{ eV}$ to a well-resolved peak for the higher energies (Fig. 6). It is worth mentioning that the plasmon

$\omega_+^{(1)}$ is shifted to the phonon peak ω_0 with the increase of the primary energy (Figs. 1 and 5), forming the single loss structure.

B. Fitting of the measured HREELS spectra with smooth self-consistent electron-density profiles

The dopant distribution of the high-doped sample 17 is considered Gaussian shaped due to the expected wider spa-

tial spreading. First, we assume an initial distribution at time $t=0$ given by the δ function

$$n_D(t, z)|_{t=0} = N_D \delta(z - z_0),$$

where N_D is the total areal density of electrically active dopant atoms and z_0 is a position of the doping plane. The solution of the diffusion equation in the presence of the non-transparent boundary at the surface for the diffusing dopants is given by

$$n_D(t, z) = \begin{cases} \frac{4N_D}{w_1 + w_2} \left(\frac{\ln 2}{\pi}\right)^{1/2} \exp\left[-\frac{(z - z_0)^2 4 \ln 2}{w_1^2}\right], & z \geq z_0 \\ \frac{4N_D}{w_1 + w_2} \left(\frac{\ln 2}{\pi}\right)^{1/2} \exp\left\{\left[-\frac{(z - z_0)^2 4 \ln 2}{w_2^2}\right] + \exp\left[-\frac{(z + z_0)^2 4 \ln 2}{w_2^2}\right]\right\}, & 0 \leq z < z_0 \end{cases} \quad (6)$$

where $w_1/2$ and $w_2/2$ are the widths of the right and the left halves of the total asymmetric Gaussian distribution, respectively, as if they are considered in the absence of the boundary. These values are related to the diffusion coefficients in both directions from the initial doping plane as

$$w_1 = 4\sqrt{\ln 2 D_1 t} \quad \text{and} \quad w_2 = 4\sqrt{\ln 2 D_2 t},$$

where D_2 and D_1 are the diffusion coefficients in the growth direction and back from the initial doping plane, respectively. Since the surface boundary restricts the diffusion process in the growth direction one obtains an accumulation of the dopants beneath the surface even in the case of the equality of the diffusion coefficients D_1 and D_2 , when the doping plane is placed close to the surface. The function in Eq. (6)

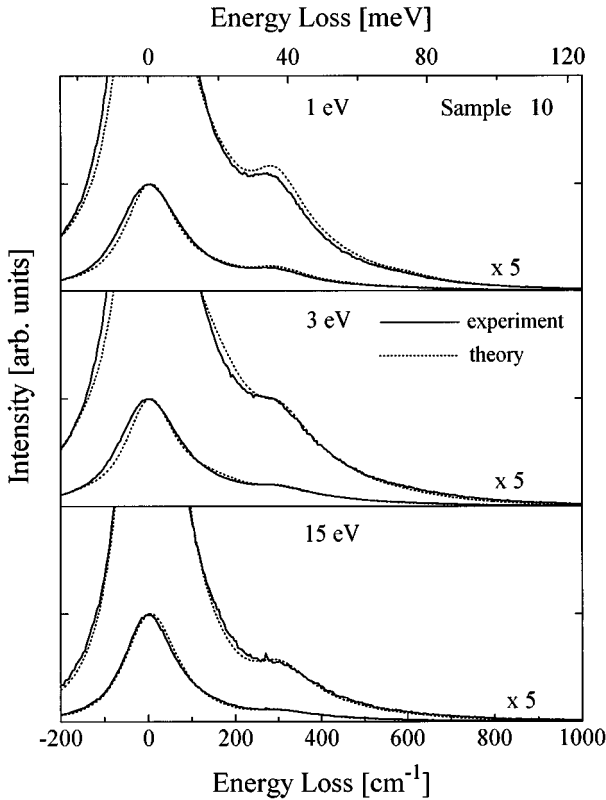


FIG. 7. The measured (solid lines) and the fitted (dotted lines) energy-loss spectra for primary beam energies $E_0=1, 3,$ and 15 eV for the low-doped sample 10 with the doping plane at a depth of 100 \AA . The rectangular-shaped dopant distribution with $w=40 \text{ \AA}$, the density of electrically active dopants $N_D=8.0 \times 10^{12} \text{ cm}^{-2}$, and the free-electron density $N_E=1.5 \times 10^{12} \text{ cm}^{-2}$ were estimated from the fitting.

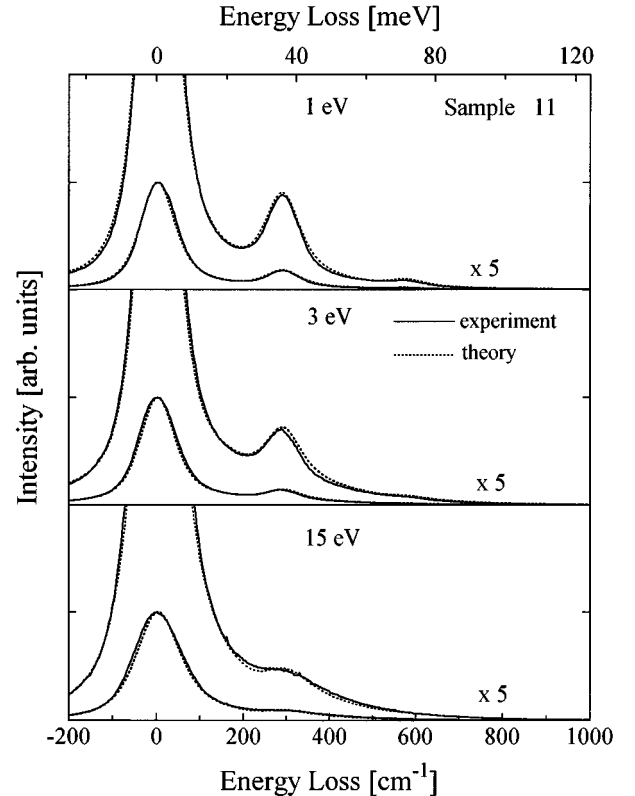


FIG. 8. The same as in Fig. 7, but for the low-doped sample 11 with the doping plane at a depth of 200 \AA . The parameters $w=80 \text{ \AA}$, $N_D=8.0 \times 10^{12} \text{ cm}^{-2}$, and $N_E=4.6 \times 10^{12} \text{ cm}^{-2}$ were estimated from the fitting.

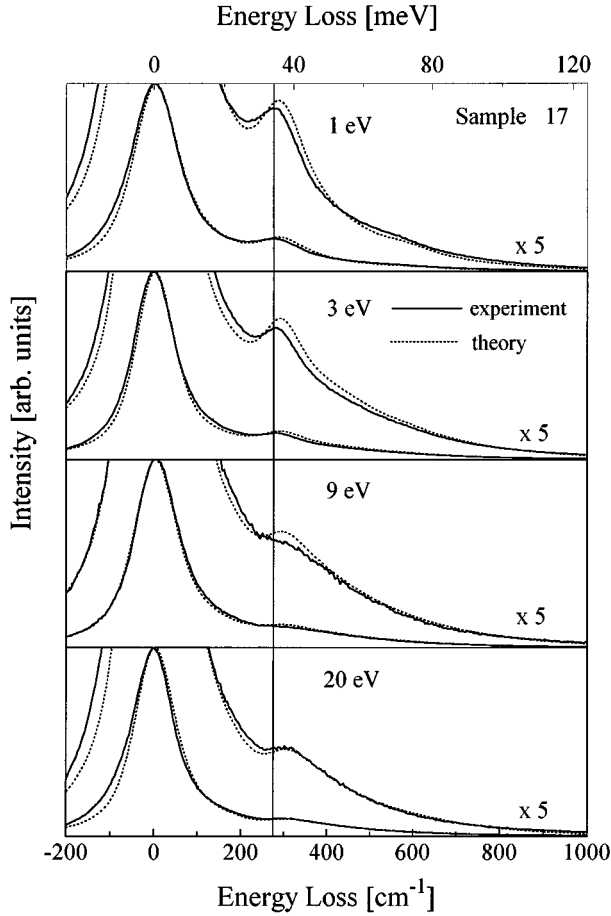


FIG. 9. The same as in Fig. 7, but for the high-doped sample 17 with the doping plane at a depth of 100 Å and for primary beam energies $E_0=1, 3, 9,$ and 20 eV. The asymmetric Gaussian-shaped dopant distribution with $w_1=100$ Å and $w_2=150$ Å was estimated.

defines an asymmetric dopant distribution, used in the self-consistent calculation of the electron-density profile, outlined in Sec. III.

As mentioned in Sec. I for the sample growth we used a temperature of 550 °C, which is lower than the temperature explored by Lohe *et al.*,¹³ and without subsequent thermal decapping of the As-passivation overlayer. For these reasons, when fitting the measured energy-loss spectra of the low-doped sample 10, based on the smooth electron-density profile, a symmetric spreading of the dopant atoms near the intended doping plane was assumed. Both rectangular and

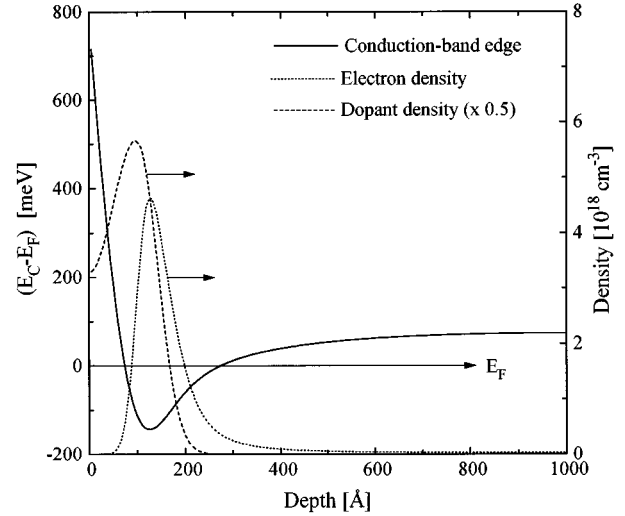


FIG. 10. The self-consistent electron-density profile (dotted line) and the conduction-band edge relative to the Fermi energy E_F (solid line) for the high-doped sample 17 with the doping plane at depth of 100 Å are displayed. The asymmetric Gaussian-shaped dopant distribution (dashed line) from equation (6) ($w_1=100$ Å, $w_2=150$ Å, $N_D=1.5 \times 10^{12}$ cm⁻²), used when solving the Schrödinger and the Poisson equations, is shown too.

Gaussian distributions of dopant atoms were used in the calculations and no notable difference was found. During the fitting, first for the primary beam energy 9 eV, we adjusted the volume density of the electrically active dopants N_D , the width of the rectangular dopant spreading w , the surface trapped charge density N_S , and the plasmon damping Γ . For the other primary beam energies only the plasmon damping was changed to obtain the best fits to the experimental data. The fitted energy-loss spectra for different primary energies are shown in Fig. 7.

The same fitting scheme was applied for the low-doped sample 11 with the intended doping plane at 200 Å depth (Fig. 8) and for the high-doped 100-Å-depth sample 17 (Fig. 9). In the latter case, we assumed the ratio w_2/w_1 of 1.5, i.e., the ratio D_2/D_1 of 2.25 between the diffusion coefficients of dopants towards the surface and backward from the doping plane, respectively. In this fashion, we simulated the preferential diffusion in the growth direction (segregation),²⁴ which is expected to be strong in the case of high doping. This results in a strong asymmetric distribution of the dopants with respect to the initial doping plane. The calculated

TABLE I. Summary of the dopant spreading parameters for the different δ -doped GaAs (100) samples (10, 11, and 17). The values listed are as follows. z_0 : depth of the initial doping plane; N_D : areal density of the electrically active dopant atoms; N_E : areal density of electrons in the conduction band; w : full width at a half maximum (FWHM) of the dopant distribution; $(E_C - E_F)_{\text{surf}}$: Schottky barrier height.

Sample	z_0 (Å)	N_D (cm ⁻²)	N_E (cm ⁻²)	w (Å)	$(E_C - E_F)_{\text{surf}}$ (eV)
10	100	8.0×10^{12}	1.5×10^{12}	40 (Rectangle)	0.72
11	200	8.0×10^{12}	4.6×10^{12}	80 (Rectangle)	0.73
17	100	1.5×10^{12}	4.9×10^{12}	$w_1=100$ $w_2=150$	0.71

TABLE II. The dependence of the plasmon damping factor Γ on the primary electron-beam energy E_0 for the different δ -doped GaAs(100) samples (10, 11, and 17). The probing depths for the phonon mode $\omega_0=36$ meV are also shown.

E_0 (eV)	Sample #10 Γ (meV)	Sample 11 Γ (meV)	Sample 17 Γ (meV)	Probing depth (\AA) for $\omega_0=36$ meV
0.5	8.7	9.9	18.6	89
1	6.0	5.0	16.1	126
3	5.6	8.7	12.4	220
6.5	31.0	14.9		325
9	26.7	21.1	21.1	382
12	19.8	22.3	21.1	441
15	19.8	27.3	17.4	493
20	13.6		21.1	570

self-consistent electron-density profile for the high-doped 100- \AA -depth sample 17 is shown in Fig. 10. It should be noted that even an approximation of the dopant spreading by a Gaussian with equal diffusion coefficients in both directions from the doping plane [Eq. (6)] can result in an appreciable asymmetry of the dopant distribution if a doping plane is positioned close to the surface.

The parameters of the dopant spreading and calculated electron-density profiles for all samples investigated are summarized in Table I.

From a detailed analysis of the results shown in Fig. 9 one can observe an appreciable shift of the main loss feature with an increase of the primary energy. Such behavior is explained by the influence of the plasmon $\omega_+^{(1)}$, which has a smaller spectral weight and is buried in the phonon peak at the low primary beam energy (top panel in Fig. 9). With the increase of the primary energy the spectral weight of the plasmon $\omega_+^{(1)}$ increases relative to the phonon mode ω_0 (Fig. 5). Accordingly, the loss feature for $E_0=20$ eV can be assigned to the plasmon mode $\omega_+^{(1)}$, disturbed by the phonon peak ω_0 . For the low-doped samples 10 and 11 the shift of the main loss feature with a variation of the primary energy is not observed due to a smaller energy separation between the phonon ω_0 and the plasmon $\omega_+^{(1)}$ peaks, respectively.

The fitted plasmon damping factors for all samples studied are presented in Table II where the probing depths of the phonon mode ω_0 are also given. The probing depth (effective spatial extent of the polarization electric field from the surface inward the bulk) can be roughly estimated¹⁷ as $1/q_{\parallel}$ with

$q_{\parallel} = (2m_0/\hbar^2)^{1/2}[E_0^{1/2} - (E_0 - \hbar\omega_0)^{1/2}] \sin \theta_f$. The most striking feature of these data is the significant decrease of the plasmon damping at the low primary energies for the low-doped samples 10 and 11 (see Table II). Such a decrease can be attributed to the spatial separation between the phonon mode, localized closely to the surface (for instance, the probing depth of the phonon mode ω_0 is 126 \AA for $E_0=1$ eV) and the plasmon mode, confined within the potential well, formed by ionized dopants at depths of 100 and 200 \AA for these two samples, respectively. One can also conclude from this finding that a scattering of plasmon excitations on the optical phonons at room temperature is dominant, if compared to the scattering on the ionized dopants. In the case of the high-doped samples the spatial separation mentioned above is less, and such a decrease of the plasmon damping was not observed.

V. CONCLUSIONS

In this paper we presented results of a HREELS investigation of the δ -doped n -type GaAs(100) samples grown at 550 $^{\circ}\text{C}$ with different doping levels and doping plane depths. From the comparison with the calculated spectra the dopant spreading has been estimated. It was shown that in low-doped samples the symmetric dopant distribution near the initial doping plane provides good fits to measured energy-loss spectra in the applied set of the primary electron-beam energies. In contrast, for high-doped samples the asymmetry in the dopant distribution was assumed to simulate a possible segregation process. This was done by virtue of the asymmetric Gaussian, which is a solution of the diffusion equation in the non-transparent surface boundary conditions for diffusing dopants.

The significant decrease of the plasmon damping at low primary beam energies for the low-doped samples is ascribed to a spatial separation between the surface optical phonon mode, strongly localized near the surface and plasmon excitations, confined within the potential well, positioned at 100 and 200 \AA from the surface for samples 10 and 11, respectively. This provides additional evidence that scattering of free electrons on the optical phonons is dominant at room temperature.²⁵⁻²⁷

ACKNOWLEDGMENTS

One of the authors (V.M.P.) gratefully acknowledges the financial support of the Heraeus foundation and of the Deutsche Forschungsgemeinschaft.

¹R. B. Beall, J. B. Clegg, and J. J. Harris, *Semicond. Sci. Technol.* **3**, 612 (1988).

²A. M. Lanzillotto, M. Santos, and M. Shayegan, *Appl. Phys. Lett.* **55**, 1445 (1989).

³E. F. Schubert, H. S. Luftman, R. F. Kopf, R.L. Headrick, and J. M. Kuo, *Appl. Phys. Lett.* **57**, 1799 (1990).

⁴Ph. Jansen, M. Meuris, M. Van Rossum, and G. Borghs, *J. Appl. Phys.* **68**, 3766 (1990).

⁵A. M. Lanzillotto, M. Santos, and M. Shayegan, *J. Vac. Sci. Technol. A* **8**, 2009 (1990).

⁶M. Santos, T. Sajoto, A. M. Lanzillotto, A. Zrenner, and M. Shayegan, *Surf. Sci.* **228**, 255 (1990).

⁷H. C. Nutt, R. S. Smith, M. Towers, P. K. Rees, and D. J. James, *J. Appl. Phys.* **70**, 821 (1991).

⁸A. Zrenner, F. Koch, and K. Ploog, *Surf. Sci.* **196**, 671 (1988).

⁹E. F. Schubert, J. B. Stark, B. Ullrich, and J. E. Cunningham, *Appl. Phys. Lett.* **52**, 1508 (1988).

¹⁰A. Zrenner, *Appl. Phys. Lett.* **55**, 156 (1989).

¹¹E. F. Schubert, R. F. Kopf, J. M. Kuo, H. S. Luftman, and P. A. Garbinski, *Appl. Phys. Lett.* **57**, 497 (1990).

- ¹²J. Wagner, M. Ramsteiner, W. Stolz, M. Hauser, and K. Ploog, *Appl. Phys. Lett.* **55**, 978 (1989).
- ¹³C. Lohe, A. Leuther, A. Förster, and H. Lüth, *Phys. Rev. B* **47**, 3819 (1993).
- ¹⁴R. Biagi and U. del Pennino, *Phys. Rev. B* **50**, 7573 (1994).
- ¹⁵S. R. Streight and D. L. Mills, *Phys. Rev. B* **37**, 965 (1988).
- ¹⁶L. Hedin and B. I. Lundqvist, *J. Phys. C* **4**, 2064 (1971).
- ¹⁷H. Ibach and D. L. Mills, *Electron Energy Loss Spectroscopy and Surface Vibrations* (Academic, New York, 1982).
- ¹⁸Ph. Lambin, J. P. Vigneron, and A. A. Lucas, *Phys. Rev. B* **32**, 8203 (1985); Ph. Lambin, J. P. Vigneron, and A. A. Lucas, *Comput. Phys. Commun.* **60**, 351 (1990).
- ¹⁹D. G. Kilday, G. Margaritondo, and G. J. Lapeyre, *J. Vac. Sci. Technol. A* **8**, 2755 (1990); Y. Chen, S. Nannarone, J. A. Schaefer, J. C. Hermanson, and G. J. Lapeyre, *Phys. Rev. B* **29**, 7653 (1989); Y. Chen, J. C. Hermanson, and G. J. Lapeyre, *ibid.* **39**, 12 682 (1989).
- ²⁰J. Lindhard, *K. Danske Videns. Selsk. Mat.-Fys. Medd.* **8**, 28 (1954).
- ²¹A. Many, I. Wagner, J. I. Gersten, and Y. Goldstein, *Phys. Rev. Lett.* **46**, 1648 (1981).
- ²²J. I. Gersten, *Surf. Sci.* **98**, 599 (1980); **92**, 579 (1980).
- ²³A. Puri and W. L. Schaich, *Phys. Rev. B* **31**, 974 (1985).
- ²⁴E. F. Schubert, J. M. Kuo, R. F. Kopf, A. S. Jordan, H. S. Luftman, and A. S. Hopkins, *Phys. Rev. B* **42**, 1364 (1990).
- ²⁵K. Hirakawa and H. Sakaki, *Phys. Rev. B* **33**, 8291 (1986).
- ²⁶P. J. van Hall, T. Klaver, and J. H. Wolter, *Semicond. Sci. Technol.* **3**, 120 (1988).
- ²⁷W. Walukiewicz, H. E. Ruda, J. Lagowski, and H. C. Gatos, *Phys. Rev. B* **30**, 4571 (1984).